

The Making of FR Is

I. Numerical Hydrodynamic 3D Simulations of Low Power Jets

S. Massaglia¹, G. Bodo², P. Rossi², S. Capetti² and A. Mignone¹

¹ Dipartimento di Fisica, Università degli Studi di Torino, via Pietro Giuria 1, 10125 Torino, Italy

² INAF/Osservatorio Astrofisico di Torino, via Osservatorio 20, 10025 Pino Torinese, Italy

Received ?? / Accepted ??

ABSTRACT

Context. Extragalactic radiosources have been classified in two classes, Fanaroff-Riley I and II, which differ in morphology and radio power. Strongly emitting sources belong to the edge brightened FR II class while the weak ones to the edge darkened FR I class. The origin of this dichotomy is not yet fully understood. Numerical simulations are successful in generating FR II morphologies but they fail to reproduce the diffuse structure of FR Is.

Aims. By means of hydro-dynamical 3D simulations of supersonic jets, we investigate how the displayed morphologies depend on the jet parameters. Bow shocks and Mach disks at the jet's head, likely responsible for the presence of hot spots in the FR II sources, disappear for a jet kinetic power $\mathcal{L}_{kin} \lesssim 10^{43}$ erg s⁻¹. This threshold compares favorably with the luminosity at which the FR I/FR II transition is observed.

Methods. The problem is addressed by numerical means carrying out three-dimensional HD simulations of supersonic jets that propagate in a non homogeneous medium with the ambient temperature that increases with distance from the jet origin, maintaining pressure constant.

Results. In the lower power sources, the jet energy, instead of being deposited at the terminal shock, is gradually dissipated by the turbulence. The jets spreads out while propagating, it smoothly decelerates while mixing with the ambient medium and produces the plumes characteristic of FR I objects.

Conclusions. Three-dimensionality is an essential ingredient to explore the FR I evolution, because the properties of turbulence in two and three dimensions are very different, since in two dimensions there is no energy cascade to small scales and two-dimensional simulations with the same parameters, lead to FR II like behavior.

Key words. Hydrodynamics, Methods: numerical, Galaxies: jets, Turbulence

1. Introduction

The extragalactic radio sources have been classified into two categories (Fanaroff & Riley 1974) based upon their radio morphology: a first class of objects, named Fanaroff-Riley I (FR I), preferentially found in rich clusters and hosted by weak-lined galaxies, shows jet-dominated emission, two-sided jets at the kiloparsec scale that smoothly extend into the intracluster medium forming large scale plumes or tails of diffuse radio emission; a second one, named Fanaroff-Riley II (FR II or “classical doubles”), found in poorer environments and hosted by strong emission-line galaxies, presents lobe-dominated emission, one-sided jets at the kpc scale that abruptly terminate into hot-spots of emission.

Besides morphology, FR I and FR II radio sources were discriminated in power as well: objects below $\sim 10^{25} h_{70}^2$ W Hz⁻¹ str⁻¹ at 178 MHz were typically found to be FR I sources. A perhaps more illuminating criterion has been found by Ledlow & Owen (1996) who plotted the radio luminosity at 1.4 GHz against the optical absolute magnitude of the host galaxy: they found the bordering line of FR I to FR II regions correlating as $L_R \propto L_{opt}^{1.7}$, i.e. in a luminous galaxy more radio power is required to form a FR II radio sources. This correlation is important since it can be interpreted as an indication that the environment may play a crucial role in determining the source structure. Further-

more, a class of hybrid sources showing a FR I structure on one side of the radio source and a FR II morphology on the other, have been discovered (Gopal-Krishna & Wiita 2000). The above arguments yield the basic question of the origin of FR I/FR II dichotomy, whether intrinsic or ambient driven (Gopal-Krishna & Wiita 2000; Wold et al. 2007; Kawakatu et al. 2009; Massaglia 2003).

Recent studies based on the cross correlation of wide area optical and radio surveys (Best & Heckman 2012) unveiled the presence of yet another class of compact radio-galaxies representing the majority of the local radio loud AGN population. Because they lack of the prominent extended radio structures characteristic of the other FR classes they were dubbed “FR 0” (Baldi & Capetti 2009, 2010; Sadler et al. 2014; Baldi et al. 2015). Nonetheless, FR 0s often show radio jets, but extending at most a few kpc (Baldi et al. 2015). This suggests that in most radio-loud AGN, the jets fail to propagate to (or become too faint to be detected at) radii exceeding the size of their host.

The distorted, diffuse and plume-like morphologies of FR I sources led to model them as turbulent flows (Bicknell 1984, 1986; Komissarov 1990a,b; De Young 1993), while the characteristics of FR II, like their linear structure and the presence of hot-spots at the jet termination, are associated to hypersonic flows. The difference in morphology between the two classes therefore reflects a difference in how the jet

energy is dissipated during jet propagation: in the first case, the jet gradually dissipates its energy and is characterized by entrainment of the ambient material, while, in the second case, the jet keeps its velocity and dumps all its energy at its termination, forming the observed hot-spots. While the dynamics of high Mach number jets has been widely studied by means of numerical simulations in 2D and 3D, e.g. Massaglia et al. (1996); Zanni et al. (2003); Hardcastle & Krause (2013, 2014), 3D simulations of transonic jets have been carried out following the evolution of instabilities to turbulence (Basset & Woodward 1995; Hardee et al. 1995; Loken 1997; Bodo et al. 1998), and simulations of turbulent jets that include the jet head propagation are limited to Nawaz et al. (2014, 2016) who investigated the properties of the jet in Hydra A, with this paper we therefore intend to start a systematic study of such flows. We perform three-dimensional simulations of the propagation of low Mach number jets in a stratified medium, that is meant to model the interstellar-intracluster transition. In this first paper we perform hydrodynamic simulations, neglecting the effects of magnetic field.

An important point to consider is that both FR I and FR II radiosources show evidence of relativistic flows at the parsec scale and therefore a deceleration to sub-relativistic velocities must occur in FR I's between the inner region and the kiloparsec scale (Giovannini et al. 1994, 2001; Laing & Bridle 2014). Several models have been proposed for the deceleration mechanism (Bicknell 1994, 1995; Komissarov 1994; Bowman et al. 1996; De Young 2005) and numerical simulations of these processes have been performed (Percucho & Martí 2007; Rossi et al. 2008; Tchekhovskoy & Bromberg 2016). In this paper, however, we assume that the deceleration has already taken place and we consider a scale where the jet is non relativistic. Moreover we want to stress that, in order to study the transition to turbulence and the turbulent structure of such flows it is essential to perform the simulations in three dimensions, in fact the behavior of 2D jets with the same physical parameters results to be completely different from their 3D counterparts.

The plan of the paper is the following: in Section 2 we describe the numerical setup and show the equations we solve, Section 3 outlines the observational framework and constrain the physical parameters, in Section 4 we present and discuss the obtained results. The conclusions are drawn in Section 5.

2. Numerical setup

2.1. Equations and Method of Solution

For the present purposes, we solve the Euler equations of gasdynamics which can be written, in quasi-linear form, as

$$\frac{\partial \rho}{\partial t} + \nabla \cdot (\rho \mathbf{v}) = 0, \quad (1)$$

$$\frac{\partial \mathbf{v}}{\partial t} + (\mathbf{v} \cdot \nabla) \mathbf{v} = -\frac{1}{\rho} \nabla P, \quad (2)$$

$$\frac{\partial P}{\partial t} + \mathbf{v} \cdot \nabla P + \Gamma P \nabla \cdot \mathbf{v} = 0, \quad (3)$$

$$\frac{\partial f}{\partial t} + \mathbf{v} \cdot \nabla f = 0. \quad (4)$$

The quantities ρ , P , \mathbf{v} are the density, pressure and velocity respectively and $\Gamma = 5/3$ is the ratio of the specific heats. The jet and the external material are distinguished using a passive tracer, f , set equal to unity for the injected jet material and equal to zero for the ambient medium. Note the the choice of $\Gamma = 5/3$ is consistent with a supersonic, nonrelativistic jets with Mach numbers > 4 (see discussion below).

Eqns (1)-(4) are solved using the Piecewise Parabolic Method (PPM) of the PLUTO code (Mignone et al. 2007, 2012) and the HLLC Riemann solver.

2.2. Initial and boundary conditions

The 3D simulations were carried out on a Cartesian domain with coordinates in the range $x \in [-L/2, L/2]$, $y \in [0, L_y]$ and $z \in [-L/2, L/2]$ (lengths are expressed in units of the jet radius r_j and y is the direction of jet propagation). At $t = 0$, the domain is filled with a perfect gas at uniform pressure but spherically stratified according to a King-like profile in density:

$$\rho(r) = \frac{1}{\eta} \frac{1}{1 + (r/r_c)^\alpha}, \quad (5)$$

where the density is expressed in units of the jet density ρ_j , $r = \sqrt{x^2 + y^2 + z^2}$ is the spherical radius, r_c is the core radius, and η is the ratio ρ_j/ρ_c between the jet density and the core density. We will set $r_c = 40r_j$ throughout and we will consider different values of the parameters α and η . The ambient temperature increases with radius as

$$T \propto 1 + (r/r_c)^\alpha \quad (6)$$

for maintaining the pressure uniform.

We impose zero-gradient boundary conditions on all computational boundaries with the exception of the injection region located at $y = 0$. Here we prescribe, inside the unit circle, a constant cylindrical inflow directed along the y direction and, in all but one case (see Table 1), in pressure equilibrium with the ambient. The inflow jet values are simply given by

$$\begin{aligned} \rho_j &= 1, \\ v_{y,j} &= M, \\ p_j &= 1/\Gamma, \\ f_j &= 1, \end{aligned} \quad (7)$$

where velocity is measured in units of the jet sound speed on the axis, $c_{s,j}$, therefore M represents the jet Mach number, and pressure is measured in units of $\rho_j c_{s,j}^2$. Outside the jet nozzle, reflective boundary conditions hold. To avoid sharp transitions, we smoothly join the injection and reflective boundary values in the following way:

$$Q(x, z, t) = Q_r(x, z, t) + \frac{Q_j - Q_r(x, z, t)}{\cosh[(R/R_s)^n]} \quad (8)$$

where $Q = \{\rho, v_x, \rho v_y, v_z, p, f\}$ are primitive flow quantities with the exception of the jet velocity which is replaced by the y -momentum while $R = \sqrt{x^2 + z^2}$ is the

cylindrical radius. Note that $Q_r(x, z, t)$ are the corresponding time-dependent reflected values while Q_j are the constant injection values given by Eqns. (7). In Eq. (8) we set $R_s = 1$ and $n = 6$ for all variables but density for which we use $R_s = 1.4$ and $n = 8$. This choice ensure monotonicity in the first (ρv_y) and second (ρv_y^2) fluid outflow momenta (Massaglia et al. 1996). We have not explicitly perturbed the jet at its inlet, differently from Mignone et al. (2010). The growing non-axially symmetric modes originate from numerical noise.

The physical domain is covered by $N_x \times N_y \times N_z$ computational zones that are not necessarily uniformly spaced. For domains with a large physical size, we employ a uniform grid resolution in the central zones around the beam (typically for $|x|, |z| \leq 6$) and a geometrically stretched grid elsewhere. In the central zones we have a resolution of 10 grid points per jet radius for the cases of $M = 4, 10$ and 13 for the case of $M = 40$. As shown in Anjiri et al. (2014), a resolution of 12 points per jet radius produces results which agree well, within few percents, with computations performed doubling this resolution. The comparison between different resolutions were carried out considering both the morphological and the energy budget aspects. The complete set of parameters for our simulations is given in Table 1.

3. Observational background and parameter constraints

In order to get physical values from the results of our simulations, we need to put constraints, derived from observational data, to the values of the fundamental units of length r_j , density ρ_j and velocity c_{sj} .

As discussed in the introduction, FR I jets propagate at relativistic velocities close to the central AGNs, at the parsec scales, while are non, or weakly, relativistic at the kiloparsec scales (Giovannini et al. 1994, 2001). Thus a jet braking process must have taken place between the inner and the outer scales (Rossi et al. 2008; Laing & Bridle 2014). Our goal here is however not to study this deceleration process, but to consider the jet propagation at scales starting from a few hundreds of pc, where the jet is already non-relativistic, to the typical linear size of FR I radio sources, ranging from about 10 up to about hundred of kiloparsec (Parma et al. (1987) for the B2 catalog sources).

At these spatial scales, the jet propagates in the galactic interstellar medium for the first few kiloparsec before exiting into the intracluster medium. The jet radius in most of FR I sources is at the limits of the angular resolution of radio interferometers such as the VLA, $\sim 0.1 - 0.3''$ (Parma et al. 1987). We assume a "fiducial" value for the jet radius $r_j = 100$ pc. We can observe that a consistent limit on the jet radius is also determined by requirements on numerical resolution: since we want the grid physical extension to be of the order of ten kiloparsec, with the given grid size, the jet radius cannot be much smaller than 100 pc, if we want to cover it with a number of points not much smaller than 10. In the following, the values of the spatial coordinates will be given in kiloparsecs, within this assumption for the initial jet radius.

The typical galactic core radius r_c attains values of the order of a few kiloparsec, and we assume $r_c = 4$ kpc, thus 40 jet radii. X-ray observations show (Posacki et al. 2013) that

within the galactic core, average temperature of the ambient medium is $T_c \sim 0.1 - 0.3$ keV, with the particle density $n_c \sim 1 \text{ cm}^{-3}$ (Balmaverde et al. 2008). As the jet enters the intragroup/intracluster medium, the ambient gas is hotter by about one order of magnitude (Sun et al. 2009; Connor et al. 2014) and the density drops by more or less the same amount. This is consistent with assuming the parameter α , in Eq. 5, between 1 and 2.

The jet parameters can be expressed as functions of the external density, ρ_c , the external temperature, T_c , the Mach number M , the density ratio η and the ratio between jet and ambient pressure as follows:

$$\rho_j = 0.01 \left(\frac{\eta}{0.01} \right) \left(\frac{\rho_c}{1 \text{ cm}^{-3}} \right) \text{ cm}^{-3}, \quad (9)$$

$$v_j = 5.1 \times 10^8 M \left(\frac{T_c}{0.2 \text{ keV}} \right)^{1/2} \left(\frac{\eta}{0.01} \right)^{-1/2} \left(\frac{P_j}{P_c} \right)^{1/2} \text{ cm s}^{-1}, \quad (10)$$

we can also derive the jet kinetic power as

$$\mathcal{L}_{kin} = 1.1 \times 10^{42} \left(\frac{r_j}{100 \text{ pc}} \right)^2 \left(\frac{\rho_c}{1 \text{ cm}^{-3}} \right) \left(\frac{T_{ext}}{0.2 \text{ keV}} \right)^{3/2} \left(\frac{M}{4} \right)^3 \left(\frac{\eta}{0.01} \right)^{-1/2} \left(\frac{P_j}{P_c} \right)^{3/2} \text{ erg s}^{-1}. \quad (11)$$

The computational time unit τ is the sound travel time over the initial jet radius, in physical units corresponds to

$$\tau = \frac{r_j}{c_{si}} = 7.7 \times 10^4 \left(\frac{r_j}{100 \text{ pc}} \right) \left(\frac{T_c}{0.2 \text{ keV}} \right)^{-1/2} \left(\frac{\eta}{0.01} \right)^{1/2} \left(\frac{P_j}{P_c} \right)^{-1/2} \text{ yrs}. \quad (12)$$

Our typical simulation covers about 100 to 1000 time units, corresponding to about $10^7 - 10^8$ yrs of the source lifetime, while it has traveled more than 10 kpc in the ambient medium.

Various methods to convert the kinetic jet power \mathcal{L}_{kin} into observed radio luminosity L_r have been proposed; we are here mainly interested into an estimate of \mathcal{L}_{kin} corresponding to the power at which the FR I/FR II transition occurs, \mathcal{L}_{trans} . Willott et al. (1999) obtained a relation according to which \mathcal{L}_{kin} scales as $L_r^{6/7}$, leading to $\mathcal{L}_{trans} \sim 1.4 \times 10^{43} \text{ erg s}^{-1}$. Birzan et al. (2004) estimated \mathcal{L}_{kin} from the observations of the X-ray cavities inflated by radio AGN. The value of \mathcal{L}_{trans} based on their calibration support the above estimate returning values in the range $\mathcal{L}_{trans} \sim 3 \times 10^{42} - 5 \times 10^{43} \text{ erg s}^{-1}$ at the FR I/FR II power transition.

We will perform various simulations, described in the following section, starting at $\mathcal{L}_{kin} = 1.1 \times 10^{42} \text{ erg s}^{-1}$, within the expected range of FR I power, and then increasing the jet power into the FR II regime.

Table 1. Parameter set used in the numerical simulations.

| 1 | 2 | 3 | 4 | 5 | 6 | 7 | 8 | 9 | 10 | 11 |
|---|-----------|-----|----------|-----------|-------------------|-----------------------------|-----------------------------|------------------------------|--------------------|----|
| | η | M | α | P_j/P_c | v_j (cm/s) | \mathcal{L}_{kin} (erg/s) | $L_x \times L_y \times L_z$ | $N_x \times N_y \times N_z$ | Notes | FR |
| A | 10^{-2} | 4 | 0 | 1 | 5.1×10^8 | 1.1×10^{42} | $64 \times 120 \times 64$ | $512 \times 1280 \times 512$ | Not stratified | I |
| B | 10^{-2} | 4 | 2 | 1 | 5.1×10^8 | 1.1×10^{42} | $64 \times 120 \times 64$ | $512 \times 1280 \times 512$ | Reference case | I |
| C | 10^{-2} | 4 | 1 | 1 | 5.1×10^8 | 1.1×10^{42} | $64 \times 120 \times 64$ | $512 \times 1280 \times 512$ | Different α | I |
| D | 10^{-2} | 4 | 2 | 10 | 1.6×10^9 | 3.5×10^{42} | $64 \times 120 \times 64$ | $512 \times 1280 \times 512$ | Overpressured | I |
| E | 10^{-2} | 40 | 2 | 1 | 5.1×10^9 | 1.1×10^{45} | $60 \times 240 \times 60$ | $576 \times 2560 \times 576$ | Highest power | II |
| F | 10^{-2} | 10 | 2 | 1 | 1.3×10^9 | 1.7×10^{43} | $64 \times 120 \times 64$ | $512 \times 1280 \times 512$ | Interm. power | II |
| G | 10^{-3} | 4 | 2 | 1 | 1.6×10^9 | 3.5×10^{42} | $64 \times 120 \times 64$ | $512 \times 1280 \times 512$ | Lighter jet | I |

Column description: 1) case identifier, 2) density ratio η , 3) Mach number M , 4) exponent α characterizing the initial density distribution, 5) ratio between jet and external pressure, 6) jet velocity, 7) jet kinetic power, 8) domain extension in the three directions, 9) number of grid points in the three directions, 10) short description of the case, 11) resulting FR morphology. Jet velocity and kinetic power are computed with the reference values for the external medium parameters (see Section 3).

4. Results and discussion

We have carried out a series of simulation runs to explore the effects of the different parameters on the jet propagation, evolution and resulting morphologies.

Although we will simulate jets propagating in a stratified medium, reproducing the real ambient medium of radiogalaxies, we start our analysis with an initial simulation (case A in Table 1) in which the ambient density is constant. This is motivated by the need of comparing our results with those obtained in previous works. The jet has a Mach number $M = 4$ and a density contrast of $\eta = 10^{-2}$ corresponding to $\mathcal{L}_{kin} = 1.1 \times 10^{42}$ erg s $^{-1}$, well below the FR I/FR II power transition. The outcome of the simulation is presented in the 3D image shown in Fig. 1. After an initial collimated phase, the jet disrupts and expands into the ambient medium. We are presenting an image of the jet tracer and not of emission, but it can be envisaged that this diffuse gas distribution will give rise to a FR I radio morphology.

This is confirmed by Fig. 2 in which we show the maximum pressure on a transverse (xz) plane at a given position y along the jet as a function of y . The pressure rises along the jet reaching its maximum at $r \sim 40$ and then it steadily decreases. At the jet head there is only a small increase, $\sim 20\%$, indicating the presence of a weak shock.

We simulated a jet described by the same parameters but in 2D cylindrical geometry (axisymmetric), see Fig. 3, and the results are radically different. The jet remains collimated over its whole length. The pressure displays several local maxima associated with the jet internal shocks and, more importantly, with its head.

This can be explained by remembering that the properties of turbulence in two and three dimensions are very different since, in two dimensions, we don't have the energy cascade to small scales. Consequently the entrainment properties and the jet evolution result to be strongly diversified. In particular, the FR I morphology resulting from the propagation of a low power jet arises and can be explored only with 3D simulations of high resolution. In order to extract physical information from our simulations in a more realistic framework, all the cases that follow are carried out in the stratified medium described in Section 2.

In Fig. 4, top panel, we show a cut in the (y, z) plane of the logarithmic density distribution for the case B of Table

1 ($M = 4$, $\eta = 10^{-2}$, the same parameters of case A but including the external density stratification) at 5.2×10^7 yrs of lifetime of the jet and a traveled distance of 12 kpc. The general features are very similar to those shown by case A, without ambient gas stratification. We can see that there is no sign of the head Mach disk and the jet smoothly mixes with the ambient medium. This is confirmed by the cuts of the tracer distribution and of the longitudinal velocity of the matter belonging to the external medium, i.e. the quantity $(1 - f) \times v_y$, in Fig. 4, central and bottom panels. Note also that the bow shock has disappeared from the ambient medium since the head propagation has become subsonic at these distances. The jet remains well collimated out to 30-40 jet radii¹ it then rapidly widens at large distances. At the same location it decelerates and entrains external material that is also globally accelerated. This behavior is preserved qualitatively out to the jet head, with just a further widening and deceleration.

As first pointed out by Bodo et al. (1994) studying the nonlinear temporal evolution of jet velocity shear instabilities (Kelvin-Helmholtz instabilities) in 2D cylindrical symmetry and then by Bodo et al. (1998) in the 3D extension of this investigation, the evolution of unstable modes follows a trend that is essentially unchanged in the general features and that develops in three phases: 1) a first *linear phase* where the unstable modes grow according to the linear theory until internal shocks start to form; 2) this is followed by an *acoustic phase* where the growth of the internal shocks is accompanied by a global deformation of the jet, which drives shocks into the external medium, these shocks carry both momentum and energy away from the jet, and transfer these to the external medium; 3) eventually a final *mixing phase* where, as a consequence of the shock evolution, turbulent mixing between jet and the ambient medium begins. In Fig. 5 (top panel) the cut of the pressure distribution of the *external* medium, i.e. displaying the quantity $(1 - f) \times P$, is suitable to show how these three phases develop in space. In Fig. 5 (bottom panel) we show a detail of the total pressure in the central and initial section of the domain that interests the linear and, partly,

¹ This is the same value of the core radius of the external gas distribution; however, this is observed also in case A where no stratification is present and it should be considered as a coincidence. This distance is most likely related to the growth length of instabilities that cause the transition to turbulence.

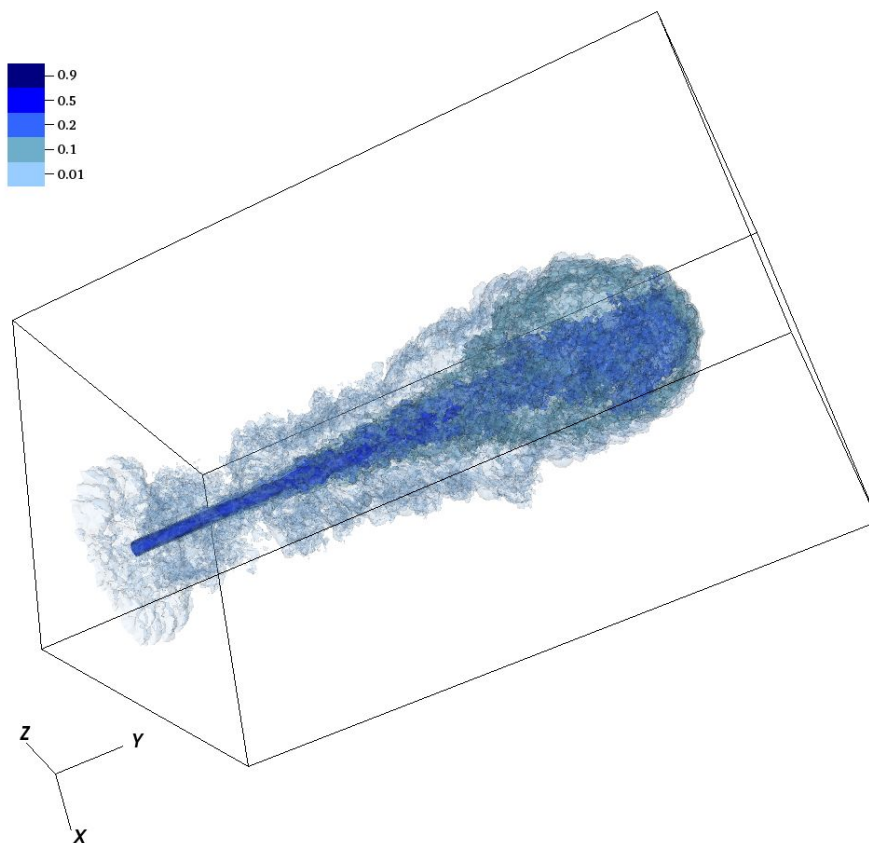


Fig. 1. 3D volume rendering of the tracer distribution for case A ($M = 4$, $\eta = 10^{-2}$, $\mathcal{L}_{\text{kin}} = 1.1 \times 10^{42} \text{ erg s}^{-1}$) at $t = 740$ time units, 5.7×10^7 yrs. The size of the computational box is $6.4 \times 12 \times 6.4$ kpc

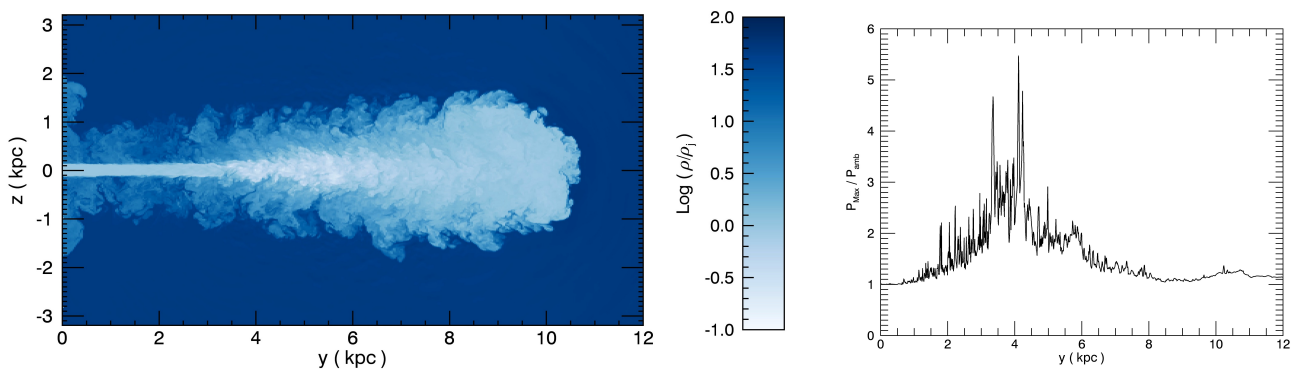


Fig. 2. Results for case A ($M = 4$, $\eta = 10^{-2}$, $\mathcal{L}_{\text{kin}} = 1.1 \times 10^{42} \text{ erg s}^{-1}$) at $t = 740$ time units, 5.7×10^7 yrs. Left: cut in the (y, z) plane of the logarithmic density distribution in units of jet density. The spatial units are in jet radii (100 pc) and the image extends over 12 kpc in the jet direction and over 6 kpc in the transverse direction. Right: maximum pressure on a xz plane at a given position y along the jet as a function of y . The pressure is in units of the ambient value

the acoustic phase. We can note the presence of oblique shocks internal to the jet.

The main properties obtained for case B are reproduced also in case C, which differs only for the parameter α describing the density profile of the ambient medium (see Fig. 6). We note just a slightly slower (by $\sim 10\%$) advance of the jet head due to the slower density decrease of the external gas.

In the cases considered so far we assumed that the jet is initially in pressure equilibrium with the ambient medium. This choice is motivated by the fact that an overpressured (underexpanded) jet develops a recollimation shock that leads to an equal pressure between the internal and external gas (Belan et al. 2010). It is likely that this occurs at radii smaller than those probed by our simulations, within the initial 100 pc of the jet length, and that the jet is already

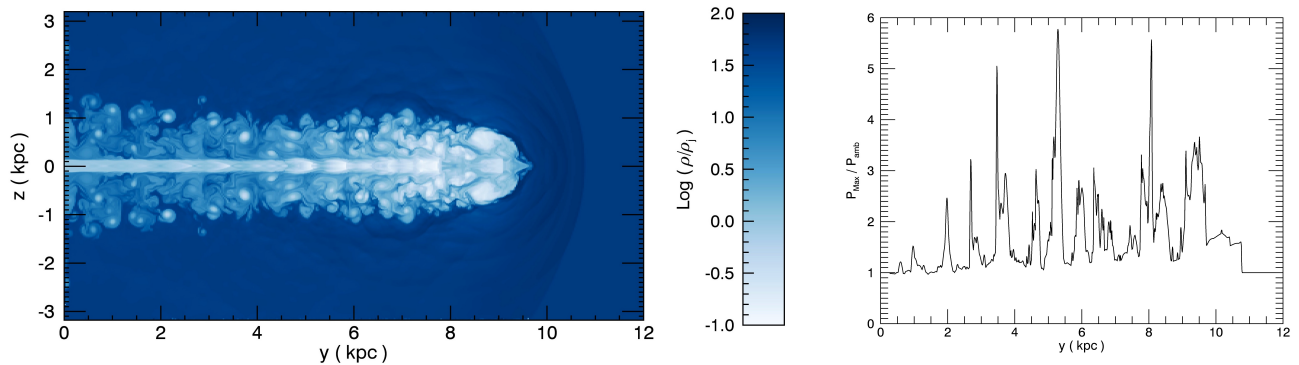


Fig. 3. Results for a 2D simulation with the same jet parameters as case A and at $t = 500$ time units, 4×10^7 yrs.

in pressure equilibrium at injection. It is nonetheless useful to assess what are the main features of the evolution of an overpressured jet that we simulated with $P_{jet}/P_{amb} = 10$, as Case D. The general morphology is similar to that of case A (see Fig. 7), but, as expected, the jet shows a recollimation shock at $r < 10$ where it has already expanded to twice its initial radius. This rapid spread causes the jet disruption to occur at smaller distances, $r \sim 20$, with respect to case A. Nonetheless, the jet advances at a very similar speed.

This investigation is characterized by two main parameters, i.e. the density ratio η and the Mach number M , as defined in Section 2. The cases presented in detail are characterized by the lowest value of kinetic power. Exploring the parameters plane, we reach higher power and we notice a transition between FR I-like to FR II-like morphologies. This becomes evident by comparing the density distributions of Fig. 2 and 8 relative to the cases A and E, respectively. Case E differs from case A only for its Mach number, 40 instead of 4, but this translates into a 1,000 larger kinetic power. Case E is characterized by the presence of a shocked region at the jet head, with the consequent cocoon that shrouds and separates the shocked region by the external unperturbed medium, characteristics typical of FR II sources.

A more quantitative representation of the differences between these two simulations is obtained by looking at the plots of the maximum pressure as functions of the longitudinal distance given in Fig. 9. In the low power case B (left panel) the pressure reaches its maximum value at ~ 40 jet radii and then it steadily decreases with only a slight increase at the jet head. In the high power case E (center panel) the maximum pressure, besides small scale peaks (likely the locations of the internal shocks), shows a large increase toward the jet termination point.

But at which Mach number does this transition occur? Maintaining η constant, we have performed a simulation with a more moderate Mach number in case F, $M = 10$ (corresponding to $\mathcal{L}_{kin} = 1.7 \times 10^{43}$). Looking at Fig. 10 we see the presence of the cocoon and of the shocked region at the jet head, as confirmed by the maximum pressure behavior in Fig. 9 (right panel), where shocks are still clearly visible. Thus, at $\eta = 0.01$ the transition between FR I and FR II morphologies occurs between $M = 4$ and $M = 10$.

Finally, we consider case G with the same Mach number ($M = 4$) of the reference case, but of lower density ($\eta = 10^{-3}$). The jet kinetic power is $\mathcal{L}_{kin} = 3.5 \times 10^{42}$, ~ 3 times higher than case B.² The resulting density distribution and pressure profile (see Fig. 11) indicates that this case corresponds to a FR I morphology.

From our simulations we recover a separation between FR I and FR II morphologies that occurs at a jet power in remarkable agreement with the observations.

Another important difference between the cases producing FR I and FR II is the advance speed of the jet. The progress of the jet into the ambient medium is shown in Fig. 12 for the case B (left panel), where the solid line represents the position of the jet head as a function of time and the dashed line, given as a reference, is obtained by the longitudinal momentum conservation at the jet head in a uniform medium (Martí et al. 1994):

$$y_{\text{head}} = \frac{M}{1 + 1/\sqrt{\eta}} t. \quad (13)$$

Note that, notwithstanding the longitudinal decrease of the ambient medium, that favors an increase of the jet propagation speed, the jet slows down because of the disruption of the Mach disk. The jet advance shows a “knee” at $t \sim 100$ time units where the velocity drops by a factor ~ 2 . After the knee the velocity approach a constant value of $v_{\text{head}} \sim 500 \text{ km s}^{-1}$.

Conversely, in case E and F (Fig. 12, center and right panel, respectively) the head progress rate increases when it reaches $r \sim 20$ due to the drop in the external density. This is because, unlike what is seen in case B, the jet remains well collimated. A subtle difference is nonetheless present as in case F the advance speed appears to decrease at $r \gtrsim 80$ were indeed the jet starts to loose its coherence, while it remains constant for the more powerful jet simulated with case E.

² It is counter intuitive that a lighter jet has a higher jet power. However, from the condition of pressure equilibrium a lighter jet is also hotter and, therefore, for the same Mach number has a larger velocity.

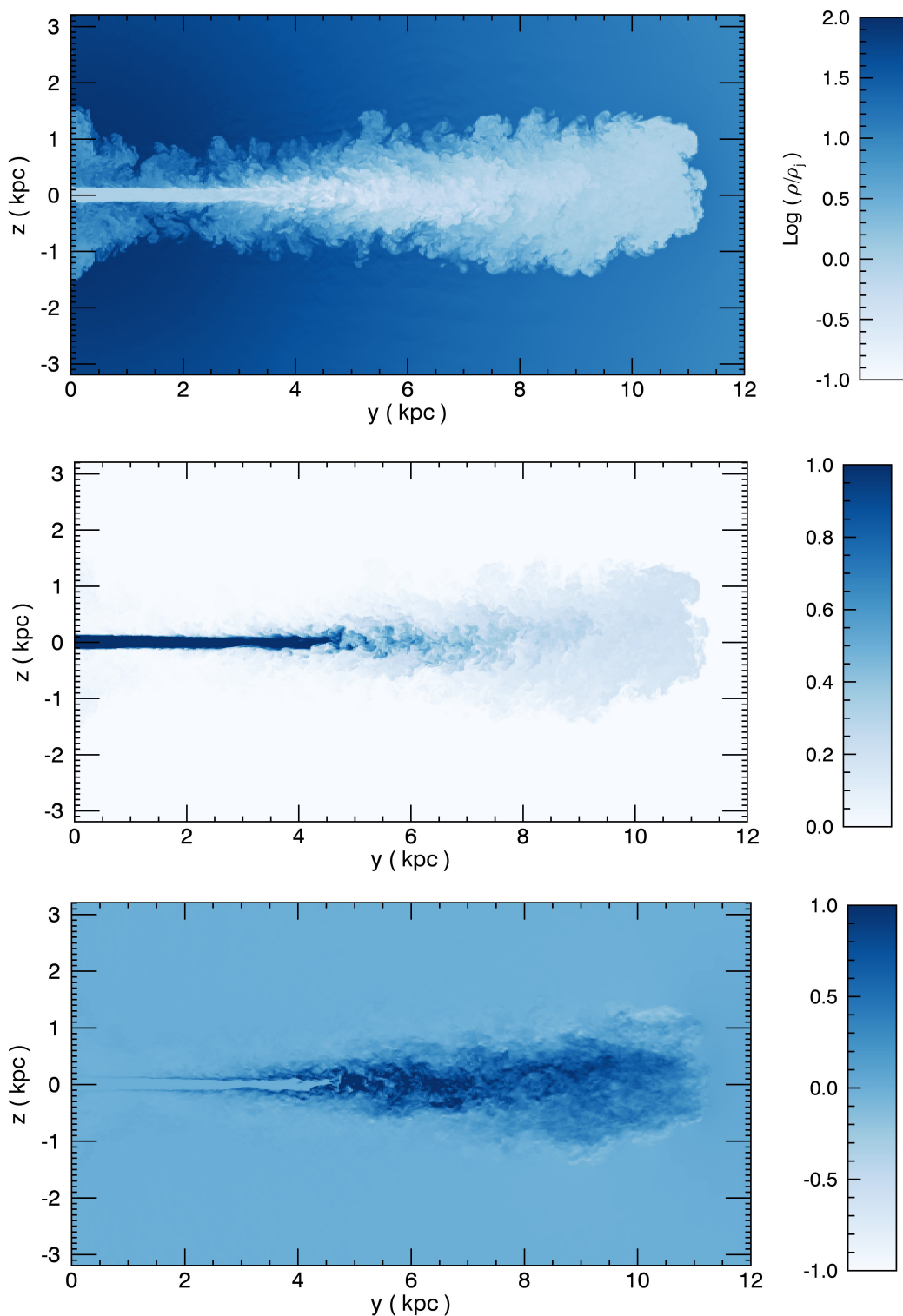


Fig. 4. Results for our reference case B ($M = 4$, $\eta = 10^{-2}$, $\mathcal{L}_{kin} \sim 1.1 \times 10^{42} \text{ ergs s}^{-1}$), at $t = 640$ time units, 4.9×10^7 yrs). The spatial units are in jet radii (100 pc) and the image extends over 12 kpc in the jet direction and over 6 kpc in the transverse direction. Cuts in the (y, z) plane of (top) the logarithmic density distribution in units of jet density, (center) tracer distribution and (bottom) distribution of the longitudinal velocity of the external medium in units of c_{sj}

5. Summary and conclusions

We have performed three-dimensional numerical simulations of turbulent jets, which give origin to morphologies typical of FR I radiosources. The jet propagates in a stratified medium that is meant to model the interstellar intra-

cluster transition. FR I radiosources are known to be relativistic at the parsec scale, therefore a deceleration to sub-relativistic velocities must occur between this scale and the kiloparsec scale. In this paper we do not model the deceleration process, but we assume that deceleration already occurred and consider scales where the jet is sub-relativistic.

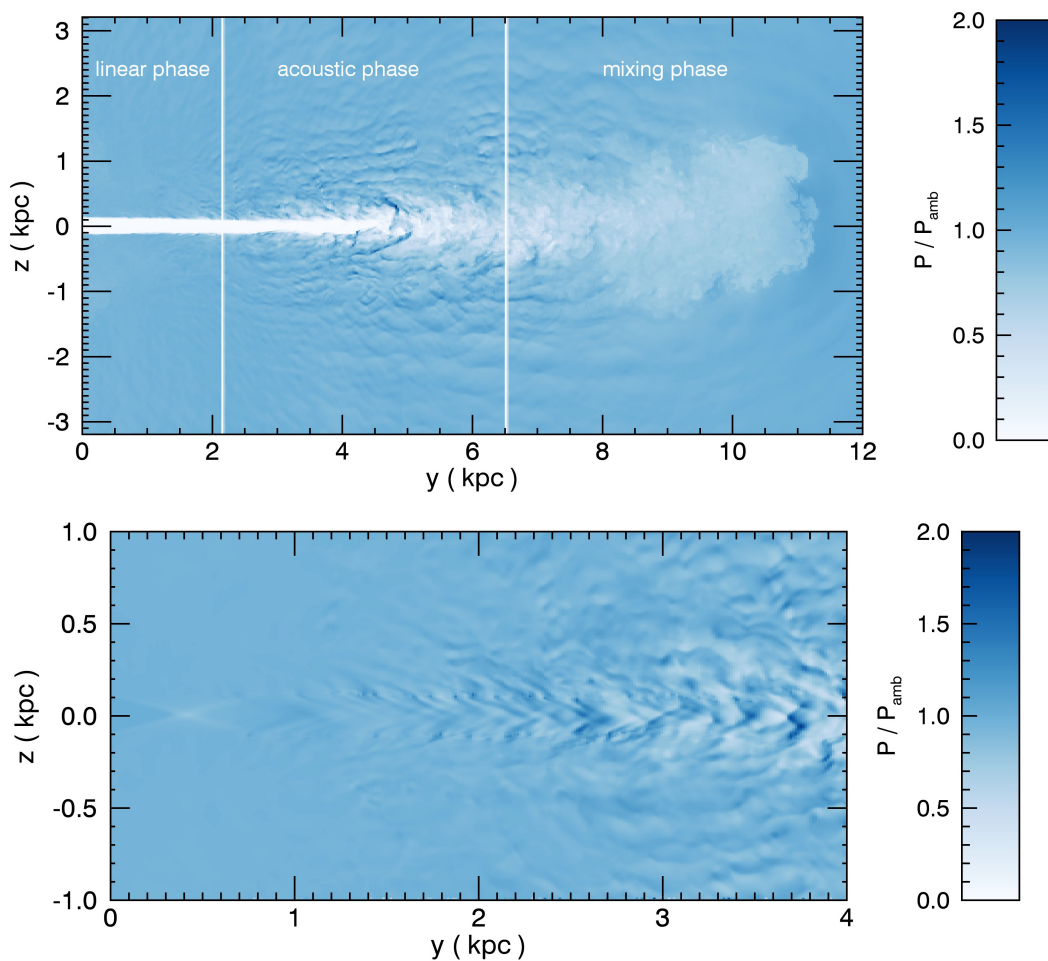


Fig. 5. The same as in Fig. 4, but for the pressure distribution of the external medium. The three phases of the evolution are labeled (top panel). The bottom panel shows the total pressure distribution in the initial part of the jet with internal shocks

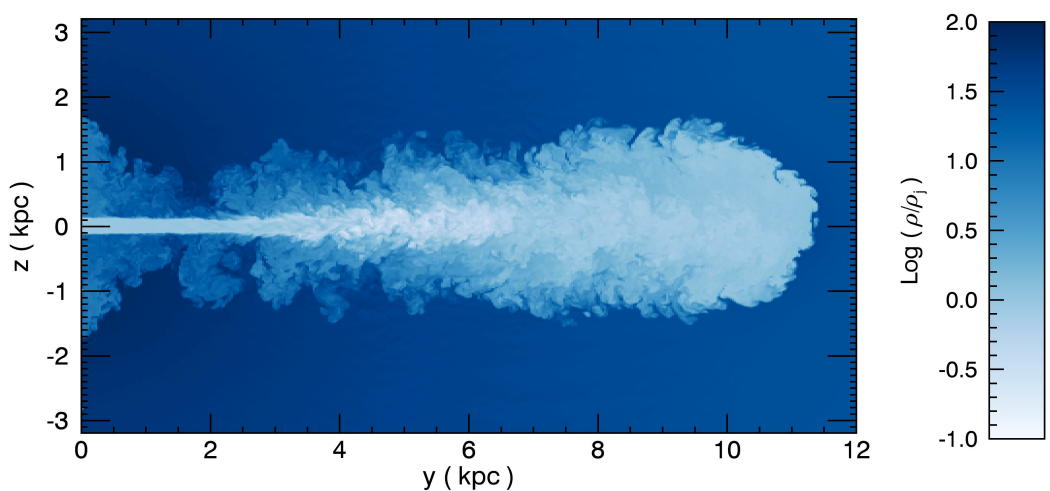


Fig. 6. Cut in the (y, z) plane of the logarithmic density distribution for the case C, differing from the reference case B for the value of α describing the external medium, at $t = 740$ time units

We did not consider buoyancy effects, by not taking into account the galaxy gravitational potential, however they should be negligible up to the distances reached by the jet's head in our simulations (of the order of ten kpc), while they

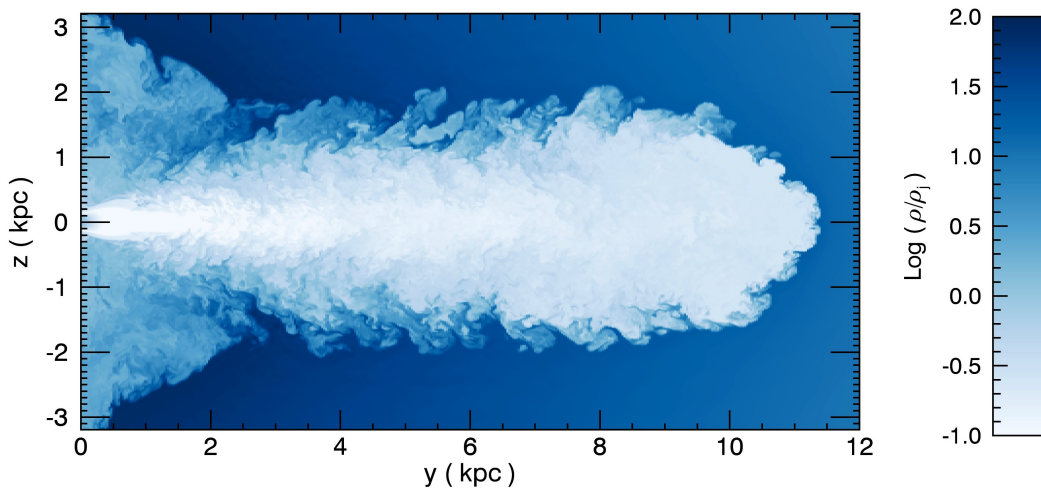


Fig. 7. Cut in the (y, z) plane of the logarithmic density distribution for the case D, overpressured jet, at $t = 720$ time units, 1.7×10^7 yrs.

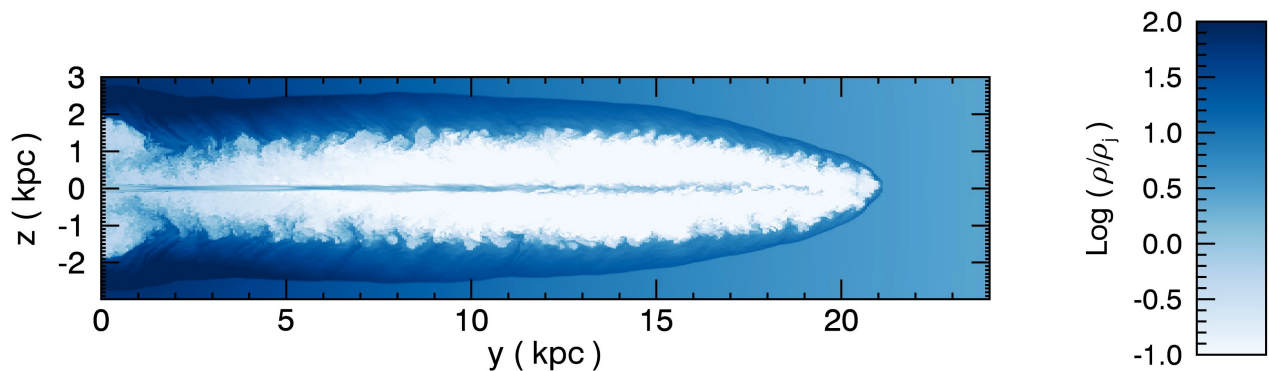


Fig. 8. Cut in the (y, z) plane of the logarithmic density distribution for the case E, the highest jet power ($M = 40$, $\eta = 10^{-2}$, $\mathcal{L}_{kin} = 1.1 \times 10^{45}$), at $t = 36$ time units, 3×10^6 yrs

may become more relevant at larger distances, as the head further slows down. In this first analysis we also neglected the effect of magnetic field, the parameters governing the jet evolution are therefore the Mach number M and the initial jet-to-ambient density ratio η , which, by constraining through observational data the values of the external density and temperature, can be combined to give the jet kinetic power.

The estimated the jet kinetic power of transition between FR I and FR II is $10^{43} \text{ erg s}^{-1}$ and we investigated a series of cases below this threshold. These low-power cases have $M = 4$ and different values of density ratio and they all give rise to turbulent structures typical of FR I sources. The jet power, instead of being completely deposited at the termination through a series of terminal shocks, as in FR II sources, is gradually dissipated by the turbulence. We showed that three-dimensionality is an essential ingredient for the occurrence of the transition to turbulence, two-dimensional simulations with the same parameters lead to FR II like behavior with energy dissipation concentrated

at the jet termination. Increasing the Mach number to 40 and consequently the kinetic power well above the FR I - FR II threshold we obviously recover well collimated jets that dump all their energy at the termination shocks. At intermediate Mach numbers ($M = 10$), with a kinetic power around the transition value, we find characteristics typical of FR II sources, even though the energy deposition at the jet termination starts to become more gradual and the morphology acquires some of the FR I properties.

The simulations presented show that in FR Is the jet's energy is transferred to the ISM in part inducing, via entrainment, a global low velocity outflow; the remaining power is instead dissipated via acoustic waves. The energy released by active nuclei is thought to play a fundamental role in the evolution of their host galaxies (Fabian 2012); in particular, in radio-loud AGN, the kinetic energy carried by their jets is transferred to the surrounding medium leading to the so-called “radio-mode” feedback. The FR I jets, although of lower power with respect to those of FR IIs, are extremely important for the point of view of feedback. This

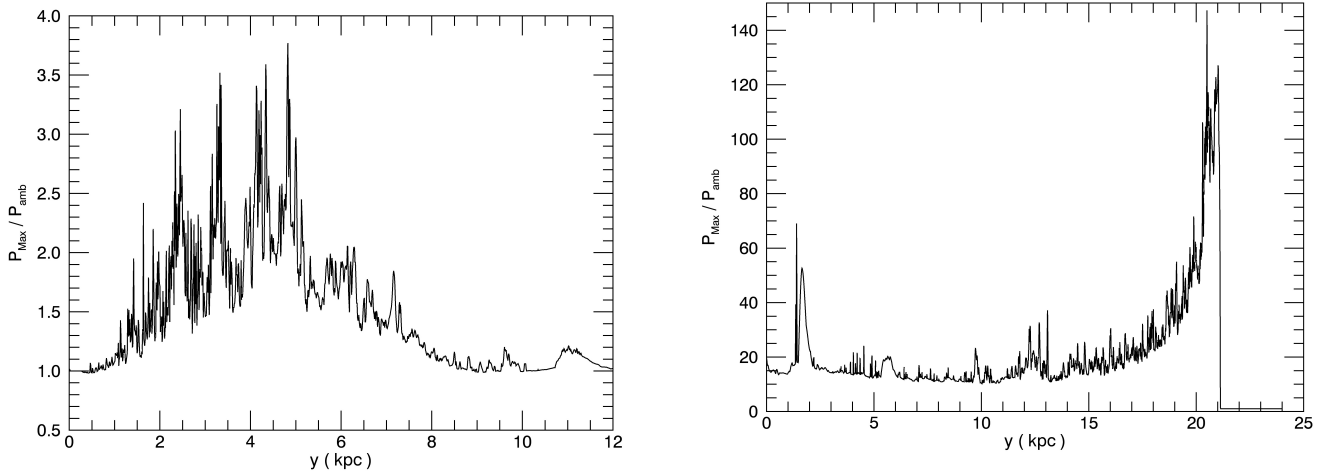


Fig. 9. Maximum pressure on transverse planes vs y for the case B at $t = 640$ time units (left panel), case E at $t = 36$ (right panel).

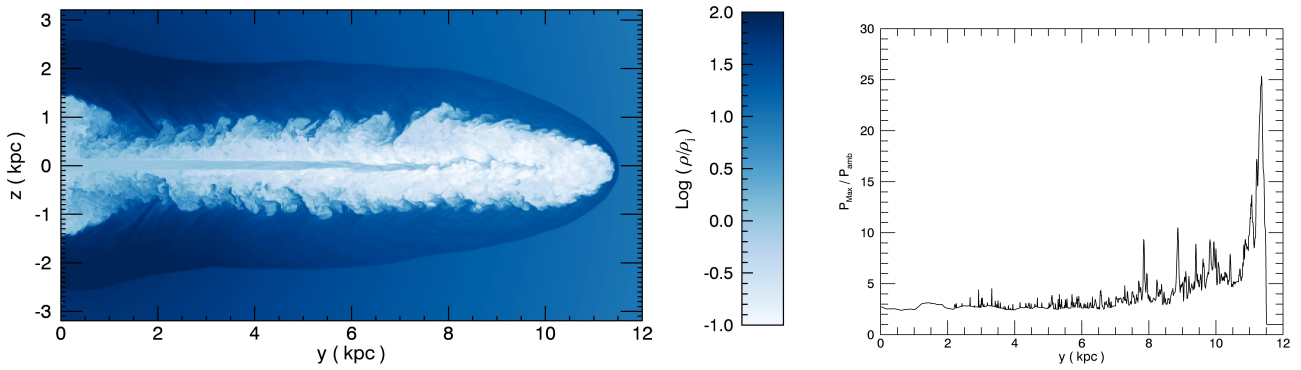


Fig. 10. Left: cut in the (y, z) plane of the logarithmic density distribution for the case F ($M = 10$, $\eta = 10^{-2}$, $\mathcal{L}_{kin} = 1.7 \times 10^{43}$) at $t = 98$ time units, 7.5×10^6 yrs; right: maximum pressure on transverse planes along the jet.

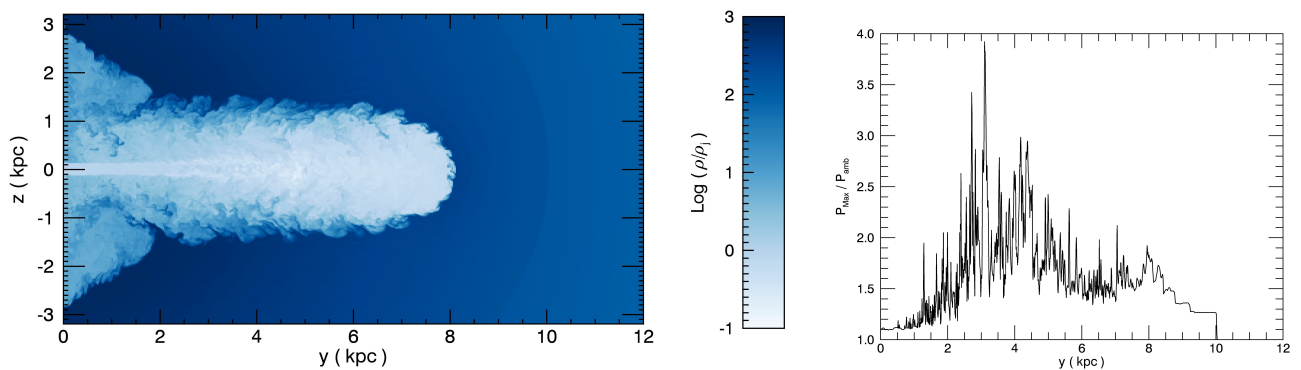


Fig. 11. Left: cut in the (y, z) plane of the logarithmic density distribution for the case G ($M = 4$, $\eta = 10^{-3}$, $\mathcal{L}_{kin} = 3.5 \times 10^{42}$) at $t = 1100$ time units, 8.5×10^7 yrs; right: maximum pressure on transverse planes along the jet.

is because the FR I jets remain confined within the central regions of the host over longer timescales (and possibly for their whole lifetime) exceeding, for our reference case B, 10^7

years. Furthermore, effectively, the whole host is affected by the “radio-mode” feedback, while in more powerful radiosources a smaller volume (immediately surrounding the

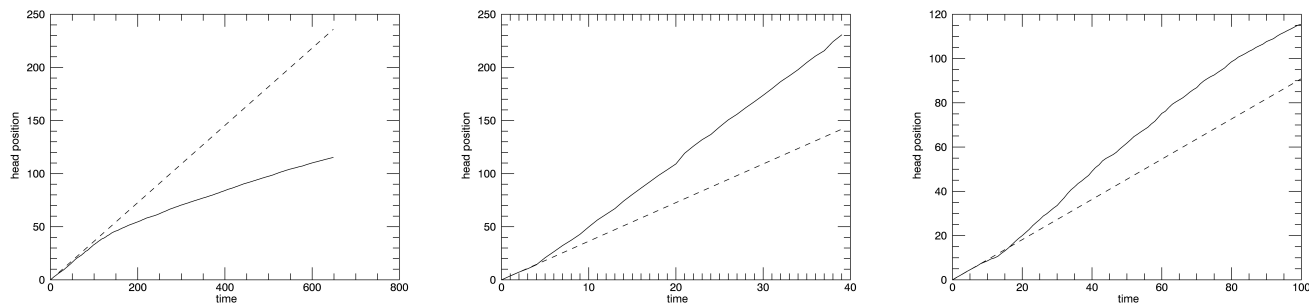


Fig. 12. Jet head position as a function of time (solid line) compared with the theoretical estimate for a uniform medium (dashed line) for the case B, E, and F in the left, center, and right panel, respectively.

jets) is involved. Finally, due to the steepness of the radio luminosity function (e.g., Mauch & Sadler 2007) the less powerful FR I radio sources are much more common than the FR II and they are then (potentially) able to affect the general evolution of massive elliptical galaxies. Clearly, further simulations are required to assess quantitatively the effects of feedback in FR Is.

Acknowledgements. The numerical calculations were performed at CINECA in Bologna, Italy, thanks to an ISCR grant.

References

- Anjiri, M., Mignone, A., Bodo, G., & Rossi, P. 2014, *MNRAS*, 442, 2228
- Baldi, R. D. & Capetti, A. 2009, *A&A*, 508, 603
- Baldi, R. D. & Capetti, A. 2010, *A&A*, 519, A48+
- Baldi, R. D., Capetti, A., & Giovannini, G. 2015, *A&A*, 576, A38
- Balmaverde, B., Baldi, R. D., & Capetti, A. 2008, *A&A*, 486, 119
- Basset, G. M. & Woodward, P. R. 1995, *ApJ*, 441, 582
- Belan, M., de Ponte, S., & Tordella, D. 2010, *Phys. Rev. E*, 82, 026303
- Best, P. N. & Heckman, T. M. 2012, *MNRAS*, 421, 1569
- Bicknell, G. V. 1984, *ApJ*, 286, 68
- Bicknell, G. V. 1986, *ApJ*, 300, 591
- Bicknell, G. V. 1994, *ApJ*, 422, 542
- Bicknell, G. V. 1995, *ApJS*, 101, 29
- Bodo, G., Massaglia, S., Ferrari, A., & Trussoni, E. 1994, *A&A*, 283, 655
- Bodo, G., Rossi, P., Massaglia, S., et al. 1998, *A&A*, 333, 1117
- Bowman, M., Leahy, J. P., & Komissarov, S. S. 1996, *MNRAS*, 279, 899
- Connor, T., Donahue, M., Sun, M., et al. 2014, *ApJ*, 794, 48
- De Young, D. S. 1993, *ApJ*, 405, L13
- De Young, D. S. 2005, in *X-Ray and Radio Connections*, ed. L. O. Sjouwerman & K. K. Dyer
- Fabian, A. C. 2012, *ARA&A*, 50, 455
- Fanaroff, B. L. & Riley, J. M. 1974, *MNRAS*, 167, 31P
- Giovannini, G., Cotton, W. D., Feretti, L., Lara, L., & Venturi, T. 2001, *ApJ*, 552, 508
- Giovannini, G., Feretti, L., Venturi, T., et al. 1994, *ApJ*, 435, 116
- Gopal-Krishna & Wiita, P. J. 2000, *A&A*, 363, 507
- Hardcastle, M. J. & Krause, M. G. H. 2013, *MNRAS*, 430, 174
- Hardcastle, M. J. & Krause, M. G. H. 2014, *MNRAS*, 443, 1482
- Hardee, P. E., Clarke, D. A., & Howell, D. A. 1995, *ApJ*, 441, 644
- Kawakatu, N., Kino, M., & Nagai, H. 2009, *ApJ*, 697, L173
- Komissarov, S. S. 1990a, *Ap&SS*, 165, 313
- Komissarov, S. S. 1990b, *Ap&SS*, 165, 325
- Komissarov, S. S. 1994, *MNRAS*, 269, 394
- Laing, R. A. & Bridle, A. H. 2014, *MNRAS*, 437, 3405
- Ledlow, M. J. & Owen, F. N. 1996, *AJ*, 112, 9
- Loken, C. 1997, in *Astronomical Society of the Pacific Conference Series*, Vol. 123, *Computational Astrophysics; 12th Kingston Meeting on Theoretical Astrophysics*, ed. D. A. Clarke & M. J. West, 268
- Martí, J. M., Mueller, E., & Ibanez, J. M. 1994, *A&A*, 281, L9
- Massaglia, S. 2003, *Ap&SS*, 287, 223
- Massaglia, S., Bodo, G., & Ferrari, A. 1996, *A&A*, 307, 997
- Mauch, T. & Sadler, E. M. 2007, *MNRAS*, 375, 931
- Mignone, A., Bodo, G., Massaglia, S., et al. 2007, *ApJS*, 170, 228
- Mignone, A., Rossi, P., Bodo, G., Ferrari, A., & Massaglia, S. 2010, *MNRAS*, 402, 7
- Mignone, A., Zanni, C., Tzeferacos, P., et al. 2012, *ApJS*, 198, 7
- Nawaz, M. A., Bicknell, G. V., Wagner, A. Y., Sutherland, R. S., & McNamara, B. R. 2016, *MNRAS*, 458, 802
- Nawaz, M. A., Wagner, A. Y., Bicknell, G. V., Sutherland, R. S., & McNamara, B. R. 2014, *MNRAS*, 444, 1600
- Parma, P., Fanti, C., Morganti, R., & de Ruiter, H. R. 1987, *A&A*, 181, 244
- Perucho, M. & Martí, J. M. 2007, *MNRAS*, 382, 526
- Posacki, S., Pellegrini, S., & Ciotti, L. 2013, *MNRAS*, 433, 2259
- Rossi, P., Mignone, A., Bodo, G., Massaglia, S., & Ferrari, A. 2008, *A&A*, 488, 795
- Sadler, E. M., Ekers, R. D., Mahony, E. K., Mauch, T., & Murphy, T. 2014, *MNRAS*, 438, 796
- Sun, M., Voit, G. M., Donahue, M., et al. 2009, *ApJ*, 693, 1142
- Tchekhovskoy, A. & Bromberg, O. 2016, *MNRAS*
- Wold, M., Lacy, M., & Armus, L. 2007, *A&A*, 470, 531
- Zanni, C., Bodo, G., Massaglia, S., Durbala, A., & Ferrari, A. 2003, *A&A*, 402, 949